Astronomy & Astrophysics

Measuring the apparent phase speed of propagating EUV disturbances

D. Yuan[1] and V. M. Nakariakov[1,2]

[1] Centre for Fusion, Space and Astrophysics, Physics Department, University of Warwick, Coventry CV4 7AL, UK
   e-mail: Ding.Yuan@warwick.ac.uk
[2] Central Astronomical Observatory at Pulkovo of the Russian Academy of Sciences, 196140 St Petersburg, Russia

ABSTRACT

Context. Propagating disturbances of the EUV emission intensity are commonly observed over a variety of coronal structures. Parameters of these disturbances, particularly the observed apparent (image-plane projected) propagation speed, are important tools for MHD coronal seismology.

Aims. We design and test tools to reliably measure the apparent phase speed of propagating disturbances in imaging data sets.

Methods. We designed cross-fitting technique (CFT), 2D coupled fitting (DCF) and best similarity match (BSM) to measure the apparent phase speed of propagating EUV disturbances in the running differences of time-distance plots (R) and background-removed and normalised time-distance plots (D).

Results. The methods were applied to the analysis of quasi-periodic EUV disturbances propagating at a coronal fan-structure of active region NOAA11330 on 27 Oct. 2011, observed with the Atmospheric Imaging Assembly (AIA) on SDO in the 171 Å bandpass. The noise propagation in the AIA image processing was estimated, resulting in the preliminary estimation of the uncertainties in the AIA image flux. This information was used in measuring the apparent phase speed of the propagating disturbances with the CFT, DCF and BSM methods, which gave consistent results. The average projected speed is measured at 47.6 ± 0.6 km s^{-1} and 49.0 ± 0.7 km s^{-1} for R and D, with the corresponding periods at 179.7 ± 0.2 s and 179.7 ± 0.3 s, respectively. We analysed the effects of the lag time and the detrending time in the running difference processing and the background-removed plot, on the measurement of the speed, and found that they are fairly weak.

Conclusions. The CFT, DCF and BSM methods are found to be reliable techniques for measuring the apparent (projected) phase speed. The samples of larger effective spatial length are more suitable for these methods. Time-distance plots with background removal and normalisation allow for more robust measurements, with little effect of the choice of the detrending time. Cross-fitting technique provides reliable measurements on good samples (e.g. samples with large effective detection length and recurring features). 2D coupled-fitting is found to be sensitive to the initial guess for parameters of the 2D fitting function. Thus DCF is only optimised in measuring one of the parameters (the phase speed in our application), while the period is poorly measured. Best similarity measure is robust for all types of samples and very tolerant to image pre-processing and regularisation (smoothing).

Key words. Sun: atmosphere – Sun: coronal mass ejections (CMEs) – Sun: UV radiation – Sun: oscillations – methods: data analysis

1. Introduction

Propagating extreme ultraviolet (EUV) intensity disturbances were discovered in the solar polar plumes (Deforest & Gurman 1998) and coronal loops (Berghmans & Clette 1999) with the Extreme ultraviolet Imaging Telescope (EIT) onboard SOlar and Heliospheric Observatory (SOHO). The follow-up studies (e.g. Ofman et al. 1999; De Moortel et al. 2000, 2002b,a; Robbrecht et al. 2001; King et al. 2003; Marsh et al. 2003; De Moortel 2009) were carried out with or in combination with the Transition Region and Coronal Explorer (TRACE, see Handy et al. 1999), which observed a part of the Sun with a better resolution, 0.5 arcsec/pixel in contrast to the 2.6 arcsec/pixel of SOHO/EIT. The propagating speeds, observed as the apparent speed projected to the image plane perpendicular to the line-of-sight (LOS) of the imagers, were normally found to be lower than the local sound speed (which can be estimated as $\simeq 152\sqrt{T[\text{MK}]} \approx 150{-}260$ km s^{-1} for the temperature T from 1 MK to 3 MK). A stereoscopic observation with the Extreme Ultraviolet Imager (EUVI, A and B) on Solar TErrestrial RElations Observatory (STEREO) revealed that the phase speed was well consistent with the sound speed inferred

from the temperature measure (Marsh et al. 2009). The propagating EUV disturbances are usually interpreted as propagating slow magnetoacoustic waves (Nakariakov et al. 2000; De Moortel 2006; Verwichte et al. 2010). Its wave nature was additionally confirmed by joint observations of intensity (density) and Doppler shift (velocity) oscillations with the EUV Imaging Spectrometer (EIS) on Hinode (Wang et al. 2009a,b; Mariska & Muglach 2010).

The amplitude of propagating EUV disturbances is normally found to be $\sim 1{-}10\%$ of the background intensity (De Moortel et al. 2002b). The low-amplitude disturbances were found to be satisfactorily modelled in the linear approximation (Nakariakov et al. 2000). The amplitude is observed to damp very quickly, typically within $2.9{-}23.3$ Mm ($1{-}2$ visible wave fronts) along the wave path (De Moortel et al. 2002b). Thermal conduction appears to be the dominant damping mechanism (De Moortel & Hood 2003; Ofman & Wang 2002; Klimchuk et al. 2004). The energy flux carried by the EUV propagating disturbances was estimated to be far too insufficient to contribute significantly to coronal heating (Ofman et al. 2000; De Moortel et al. 2002b).

Propagating EUV disturbances are usually quasi-monochromatic with the periods categorised into two classes: the

short period (∼3−5 min, see De Moortel et al. 2000, 2002b,a; De Moortel 2009; King et al. 2003; Marsh et al. 2003; Wang et al. 2009a) and long period (∼10−30 min, see Berghmans & Clette 1999; McIntosh et al. 2008; Marsh et al. 2009; Wang et al. 2009b; Yuan et al. 2011). De Moortel et al. (2002b) found statistically that the 3-min oscillations are more likely to be detected above sunspot regions, while the 5-min oscillations are usually found off the sunspots (e.g. above the plage region). This feature suggests the likely association of the coronal propagating disturbances with chromospheric 3-min oscillations and the photospheric 5-min oscillations, respectively. Chromospheric 3-min oscillations were found to leak from sunspot umbrae to the corona (Shibasaki 2001; Sych et al. 2009; Botha et al. 2011). Photospheric 5-min oscillations in plage regions are apt to be wave-guided to the corona by inclined magnetic field lines (Bel & Leroy 1977), and could be associated with the leakage of global p-modes from the photosphere (De Pontieu et al. 2005). Long-period oscillations are detected often in the corona as well, but the possible source remains poorly understood (see discussions in Yuan et al. 2011).

There are also observations of cases with multiple periods (Mariska & Muglach 2010; Wang et al. 2009b). Wang et al. (2009b) detected two harmonics in 12 and 25 min with EIS/Hinode and found that the detection length (70−90 Mm) of the long-period oscillations are much longer than previous TRACE studies (e.g. De Moortel et al. 2002b). This result is in agreement with the period-dependency of the damping length of slow magnetoacoustic wave decaying due to thermal conduction mechanism.

The apparent phase speed was measured at tens to hundreds of km s^{-1} (De Moortel et al. 2002b; De Moortel 2009). The spread of the measured speeds is usually attributed to the variation of the angle between the propagating direction and image plane in different cases. Robbrecht et al. (2001) reported that the phase speeds of propagating disturbances measured in TRACE 171 Å (1 MK) are normally lower than those measured in EIT 195 Å (1.6 MK). The temperature-dependence of the phase speed was recently found in polar plumes and the interplume medium with AIA (Krishna Prasad et al. 2011). In some cases, acceleration of the disturbances was detected at larger heights (typically above ∼20 Mm, see Banerjee et al. 2011, for a review).

Although joint imaging and spectroscopic investigations revealed that in the coronal propagating disturbances the Doppler shift is in phase with the intensity variations (Wang et al. 2009a,b; Mariska & Muglach 2010) (which is consistent with the slow magnetoacoustic wave theory, see Nakariakov et al. 2000; Tsiklauri & Nakariakov 2001), in recent studies, the observed blue-wing asymmetry in the emission spectral lines at the footpoints of coronal fan structure was interpreted in terms of periodic upflows (e.g. Doschek et al. 2007, 2008; Sakao et al. 2007; Del Zanna 2008; Harra et al. 2008; Hara et al. 2008; De Pontieu & McIntosh 2010; Tian et al. 2011a,b; Martínez-Sykora et al. 2011). A single Gaussian fit to the spectral lines suggest that the flow speed is about ∼10 km s^{-1}, much less than the observed apparent speed of propagating disturbances. Tian et al. (2011b) implemented a guided double-Gaussian fit to the spectral lines and found that the emission-line width could be associated with two components. The secondary component contributes a few percent of the total emission, its blueward asymmetry is associated with flows of speed of 50−150 km s^{-1}. The faint secondary component modulates the peak intensity, line centroid and line width quasi-periodically, therefore propagating disturbances can be observed consistently (De Pontieu & McIntosh 2010; Tian et al. 2011b). A similarity was reported between the spatial distribution of flow speed observed with Hinode/EIS and the temporal distribution of the speed of propagating disturbances observed with SDO/AIA (Tian et al. 2011b). On the other hand, the blue-wing asymmetry was found to be an intrinsic feature of upward propagating slow magnetoacoustic waves (Verwichte et al. 2010).

The typical method for studying coronal propagating disturbances is the so-called time-distance plot. In each image, a cut is taken following the direction of propagation, $F(x_i, y_j, t_k)$, where x_i and y_j are the image pixel coordinates, t_k is the time frame index. The time-distance array $C(s_m, t_k)$, where s_m is the index along the cut, is made by stacking the cuts in order of time. Propagating disturbances of the emission intensity are featured by diagonal ridges in the plot of the time-distance array (a time-distance plot). The visibility of the ridges is normally fairly poor, since EUV disturbances are weak, normally ≲10% of the background intensity, and of the same order of magnitude with the data noise. A simple and well-implemented technique, the running difference, can be applied to a time-distance plot to enhance the contrast (visibility) of the propagating disturbances. The running difference is obtained by subtracting from the cut $C(s_m, t_k)$ the value of another cut $C(s_m, t_{k-l})$ taken in the lth image ahead of the current one $R(s_m, t_k) = C(s_m, t_k) - C(s_m, t_{k-l})$. The slope of the ridges in the running distances relative to the time axis is the apparent (projected) phase speed of the propagating disturbances. Another way to enhance the visibility is to remove the quasi-static background from the image, and normalise the residue with it. The background can be obtained by temporal averaging

$$B(s_m, t_k) = \sum_{h=-N/2}^{N/2-1} C(s_m, t_{k+h})/N,$$

where N is the number of time frames. Thus, a time-distance array with background-removal and normalisation is obtained by $D(s_m, t_k) = [C(s_m, t_k) - B(s_m, t_k)]/B(s_m, t_k)$. We refer generally hereafter to the enhanced time-distance plot $X(s_m, t_k)$ as either the time-distance array made by the running difference $R(s_m, t_k)$ or the background-subtracted and normalised array $D(s_m, t_k)$.

Although a number of measurements were made on the phase speed (see De Moortel et al. 2002b,a; De Moortel 2009), no method was designed to quantify and standardise the measurement, to remove human-based bias and to make the measurements consistently comparable. The aim of this paper is to design rigorous methods for measuring the apparent phase speed of propagating disturbances in coronal imaging data, and compare their performance by the analysis of coronal propagating disturbances observed with AIA.

We describe the data pre-processing and the observation dataset in Sect. 2; the image flux error analysis is given in Sect. 3; the methods for phase speed measurement are detailed in Sect. 4; the results are summarised in Sect. 5; the conclusion is made in Sect. 6.

2. Dataset

2.1. Instrument

The *Atmospheric Imaging Assembly* (AIA, Lemen et al. 2011) onboard the *Solar Dynamics Observatory* provides continuous observations of the Sun since 2010 March 29. It images the full solar disk with 4k × 4k detectors with a resolution of
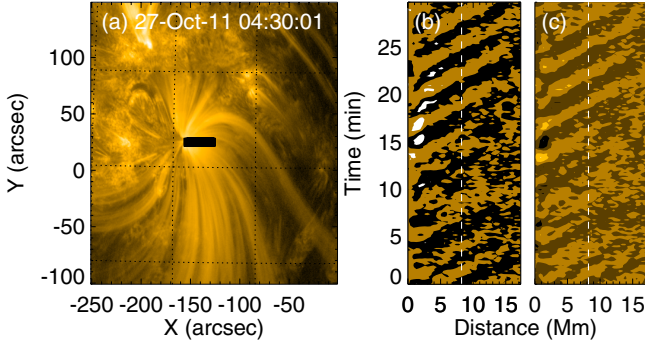
Fig. 1. a) AIA 171 Å image of active region NOAA 11330 observed on 27 Oct. 2011 at 04:30:01 UT is shown with the flux on the logarithmic scale. A cut that was taken to make the time-distance plot is indicated with a black bar. **b)** The running difference R_1 of the time-distance plot started at 04:30:01 UT. R_2 is the first half of R_1, to the left of the white dashed line. It covers about 10 cycles of the propagating features. Panel **c)** shows the background-subtracted time-distance plot D_1. The first half of D_1 on the left of the white dashed line is D_2.

0.6 arcsec/pixel. A short cadence time (~12 s) can be sustained during most of its mission. The Sun is imaged in 10 different narrow-band channels, seven of which are in EUV bandpasses: Fe xviii (94 Å), Fe viii, xxi (131 Å), Fe ix (171 Å), Fe xii, xxiv (193 Å), Fe xiv (211 Å), He ii (304 Å), Fe xvi (335 Å). The observed temperature in EUV bands ranges from ~0.6 MK to ~16 MK, and which covers the upper transition region, quiet corona, active-region corona, and flaring regions quite well.

The AIA data are stored in the level 0 format, as the raw tele-metric data compressed with the Rice algorithm. The level 1 data are obtained from level 0 (Lemen et al. 2011). In level 1 data, the digital offset of the camera, CCD readout noise and dark current are removed, a flat-field correction is applied, then the permanent bad pixels, much less than 0.1%, are detected and replaced with interpolated values from neighbouring pixels. The spikes due to energetic particles are removed with the algorithm adopted from the TRACE (Handy et al. 1999) program.

We useed level 1.5 data prepared with the subroutine *aia_prep.pro* (Version 4.11, status 2011-06-14) of SolarSoft. The images were normalised to their exposure time. A small residual roll angle between the four AIA telescopes was removed from the images. The plate scale size of the AIA images was adjusted to exactly 0.6 arcsec/pixel. Boresighting was co-aligned by adjusting the secondary mirror offset on-orbit, and the residual differences were removed by interpolating the images onto a pixel coordinate aligned with the solar centre (Lemen et al. 2011).

2.2. Observations

We used the observation dataset over a very quiescent active region (NOAA 11330) in the 171 Å bandpass at 04:00−08:00 UT on 27 Oct. 2011. No flare occurred during the observation time interval that the active region was gradually approaching the centre of the solar disk. The leading eastern part of the active region formed a fan-like feature (see Fig. 1a) that consisted of both closed and open plasma structures. Continuous propagating EUV disturbances were observed following the fan-like feature.

A four-hour dataset was downloaded as a cutout data of level 1 and prepared into level 1.5 as described in Sect. 2.1. A typical image is displayed in Fig. 1. The cadence time was very uniform, 12.000 ± 0.006 s, the exposure time was 1.9996052 ± 0.0000038 s, the total number of images in 171 Å was 1200. We truncated the size of the dataset into an array $F(x_i, y_j, t_k)$, a set

of 1200 images of 100×100 pixels, so that the fan-like structure becomes the only prominent morphological feature in the images. The images were corrected for the solar differential rotation and further co-aligned with the offsets calculated by 2D cross-correlation. The morphology of the images did not change much during the observations, either geometrically (shape) or photometrically (intensity), so the co-alignment reached a fairly good accuracy of sub-pixel.

Propagating EUV disturbances are visible along most of the strands in the fan that extends from the footpoint. We took a cut (41 pixels, ~17.7 Mm) in every image starting from the foot point and following the coronal structure extended from the west to the east (see Fig. 1). The intensity of each pixel in each image was averaged over three pixels in the vertical direction. The running difference was made with $R(s_m, t_k) = C(s_m, t_k) - C(s_m, t_{k-9})$ ($T_{lag} = t_k - t_{k-9} = 9 \times 12 = 108$ s). The running difference plot is shown in Fig. 1b. The background-subtracted normalised time-distance plot $D(s_m, t_k)$ was obtained by estimating the background with $N = 50$ smoothing ($T_{detr} = 50 \times 12 = 10$ min) and is illustrated in Fig. 1c. The propagating EUV disturbances are featured by the repeating diagonal ridges in the time-distance plot (~10 cycles during a 30-min observation). The EUV disturbances are gradually damped with height (or are buried in noise) after ~17.7 Mm along the slit. The gradient of the ridges relative to the time axis is the phase speed of EUV disturbances, projected to the image plane perpendicular to the LOS. The typical observables and physical parameters of the propagating disturbances are summarised in Table 1.

We measured the average apparent speed in the enhanced time-distance plot $X(s_m, t_k)$ with either a full (41 pixels, both the prominent part and relatively noisier part) set of pixels or its lower half (20 pixels, only the prominent part), see Fig. 1b. We prepared the enhanced time-distance plots of two sizes 41×150 and 20×150 pixels (referred to hereafter as R_1 and R_2, consequently, and R for running difference, either R_1 or R_2; D_1, D_2 and D are their analogues taken from the background-subtracted and normalised time-distance plot). R_2 (D_2) is the first half of R_1 (D_1) between 0 and 8.6 Mm along the slit, see Fig. 1a. The quality of $X(s_m, t_k)$ is quantified by two parameters: the amplitude ratio of the propagating waves and the data noise $\langle A_w \rangle / \langle A_n \rangle$, and the amplitude ratio of the propagating waves and the background intensity $\langle A_w \rangle / \langle A_b \rangle$. The amplitude is defined as the root mean square (rms),

$$\langle A_\alpha \rangle = \langle A_\alpha(s_m, t_k) \rangle = \sqrt{\sum_{m=1}^{m=N_s} \sum_{k=1}^{k=N_t} \frac{A_\alpha^2(s_m, t_k)}{N_s \times N_t}}, \quad (1)$$

where α is w, n or b for the wave, noise and background amplitude, respectively. s_m and t_k are the indices along the s and t axes, respectively. N_s and N_t are the total numbers of pixels along the axes. $N_s = 41$ or 20 for R_1 (D_1) and R_2 (D_2), respectively, and $N_t = 150$ for both of them. The array A_w is defined as $A_w(s_m, t_k) = X(s_m, t_k)$, and $A_n(s_m, t_k) = \sigma(X(s_m, t_k))$ is the data noise of $X(s_m, t_k)$ and is discussed in Sect. 3. $A_b(s_m, t_k) = B(s_m, t_k)$ is the background amplitude. The ratios $\langle A_w \rangle / \langle A_n \rangle$ are 3.3 (4.9) and 3.5 (6.9), and $\langle A_w \rangle / \langle A_b \rangle$ are 0.0145 (0.0169) and 0.0145 (0.0207), for R_1 (D_1) and R_2 (D_2), respectively.

3. Flux error analysis

3.1. AIA image noise

Although AIA outperforms TRACE (Handy et al. 1999) in FOV, cadence time and the number of observing channels, it resembles TRACE in most aspects, and many of the calibration and data

Table 1. Observables and physical parameters of the analysed propagating EUV disturbances.

Parameters	Values
Date of observation	27 Oct. 2011
Time interval of the observation	04:00:00–08:00:00 UT
Time interval of the samples	04:30:01–05:00:01 UT
Active region number	NOAA 11330
Location of the active region	$[-160'', 30'']$
Oscillation period P	$\simeq 179$ s ($\simeq 3$ min)
Apparent phase speed V_p	$\simeq 48$ km s^{-1}
Spatial wave number k	$\simeq 0.74$ Mm^{-1}
Detection distance	~ 17.7 Mm
Number of visible wave fronts	2
$\langle A_w \rangle / \langle A_b \rangle (R)$	$\sim 1.4\%$
$\langle A_w \rangle / \langle A_n \rangle (R)$	~ 3.4
$\langle A_n \rangle / \langle A_b \rangle (R)$	$\sim 0.4\%$
$\langle A_w \rangle / \langle A_b \rangle (D)$	$\sim 1.8\%$
$\langle A_w \rangle / \langle A_n \rangle (D)$	~ 5.9
$\langle A_n \rangle / \langle A_b \rangle (D)$	$\sim 0.3\%$

Fig. 2. Data noise $\sigma_{\text{noise}}(F)$ (+) in Eq. (3) as a function of pixel flux F in AIA 171 Å images. The components caused by the photon noise, compression, despiking and other reasons are plotted with $\diamond$, $\triangle$, $\square$, $\ast$ respectively.

preparation routines are adopted from the TRACE programme (Sect. 2.1). We followed the study of Aschwanden et al. (2000) on TRACE and analysed the noise in the 171 Å image flux. Data obtained in other EUV/UV channels can be analysed similarly.

In the data calibration, we neglected the uncertainties introduced by preparing the data from level 1 to 1.5, namely the errors accompanying the roll angle rotation and plate scale resizing, because the data processing is irreversible and untraceable (detached from CCD pixels). Therefore the data noise was analysed by assuming the data are of level 1 (connected to the CCD pixels). For a pixel flux value F, we combined the uncertainties generated from all the steps in units of data numbers (DN), accumulated over a fixed exposure time of 2 s, the photon Poisson noise, electronic readout noise, digitisation noise, compression noise, dark current noise, subtraction noise, and the noise due to removal of spikes in the images (Aschwanden et al. 2000):

$$\sigma_{\text{noise}}^2(F) = \sigma_{\text{photon}}^2(F) + \sigma_{\text{readout}}^2 + \sigma_{\text{digit}}^2 + \sigma_{\text{compress}}^2$$
$$+ \sigma_{\text{dark}}^2 + \sigma_{\text{subtract}}^2 + \sigma_{\text{spikes}}^2(F). \quad (2)$$

We first examine the photon statistics. The image flux in units of DN was translated from the charge readout from each pixel through an analog-to-digital converter (ADC). The camera gain (G_λ in e/DN) is defined as the number of electrons acquired in the detector to generate a unit DN read in the image pixel, it is a telescope (bandpass λ) specific parameter (Boerner et al. 2012, Table 6). The electrons are accumulated in the detector and follow Poisson statistics, thus for a pixel flux F in the image in bandpass λ, FG_λ electrons are detected with an uncertainty of $\sqrt{FG_\lambda}$, so the photon noise in F is $\sqrt{FG_\lambda}/G_\lambda = \sqrt{F/G_\lambda}$.

The intrinsic trait of CCD is the readout noise that is inevitable in all applications. The readout noise in AIA CCDs is $\approx 20-22$ e $= 1.1-1.2$ DN. For the 171 Å images, it is constant $\sigma_{\text{readout}} = 1.15$ DN (Boerner et al. 2012).

The rounding of the ADC signal into integer introduces a maximum uncertainty of $\sigma_{\text{digit}} = 0.5$ DN (Aschwanden et al. 2000).

The AIA images implement the Rice compression algorithm, a lossless compression. A look-up table was used with the bin size proportional to the pixel value (Boerner et al. 2012), thus we assume the noise $\sigma_{\text{compress}} = 0.25\sigma_{\text{photon}}$ as suggested in Boerner (2011, priv. comm.). The TRACE images deployed the *jpeg* data compression algorithm, a lossy compression algorithm. The average noise caused by the compression for the entire image was
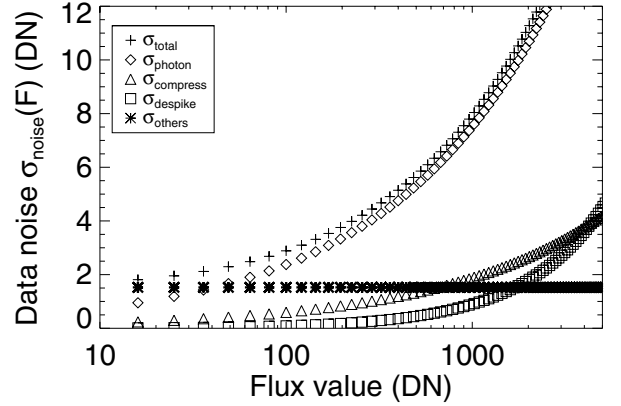
estimated as $\sigma_{\text{compress}} \lesssim 0.1$ DN (Aschwanden et al. 2000). The compression noise for TRACE was underestimated.

The noise caused by the dark current is quite low. In the current AIA operation, the seasonal variation has not be corrected yet, and we assumed a half digit noise level $\sigma_{\text{dark}} = 0.5$ DN (Boerner 2011, priv. comm.).

Subtracting the dark current, as well as the background variation, in integer DN in the data processing from level 0 to level 1, adds two additional digitisation errors, $\sigma_{\text{subtract}} = \sqrt{2 \times 0.5^2} = 0.7$ DN (Aschwanden et al. 2000).

The despiking algorithm for AIA images was directly adopted from the TRACE programme (Lemen et al. 2011), so the uncertainty analysis is transferable as well. In the deep cleaning algorithm (Aschwanden et al. 2000), if a pixel value is above $q_{\text{thresh}} = 1.15$ times its local median value (defined by the nearest eight neighbours around the spiky pixel), it would be replaced with the local median, three iterations were applied to the images. A residue of $\sigma_{\text{spikes}}(F) = F(q_{\text{thresh}} - 1) = 0.15F$ was generated in the spiky pixel and its nearest four neighbours (Aschwanden et al. 2000). In Aschwanden et al. (2000), an uncertainty of $\sigma_{\text{spikes}}(F) = 0.15F$ was assigned to each pixel empirically. In AIA images, about 10^4 pixels out of 4k × 4k are normally hit by energetic particles in quiet Sun condition (Boerner 2011, priv. comm.). As an upper limit, therefore we assumed that about 10^5 pixels (0.6%) are affected, and estimated $\sigma_{\text{spike}}(F) = 0.006 \times 0.15F = 0.0009F$ for the entire image.

Then we summarised the above estimations, the data noise for a signal pixel with the flux value F in the 171 Å images is

$$\sigma_{\text{noise}}(F) = \sqrt{(1+0.25^2)\frac{F}{17.7} + 1.15^2 + 4 \times 0.5^2 + (0.0009F)^2}$$
$$\approx \sqrt{2.3 + 0.06F} \ (\text{DN}). \quad (3)$$

The data noises of different origin in the 171 Å bandpass are plotted in Fig. 2 as a function of the image flux F. The photon noise is comparable to the other noises, caued by readout and dark current extraction and compression, at lower flux value F, and become the dominant noise at the flux value of hundreds and over. The despiking noise is practically negligible, but could become significant during a flare.

3.2. Uncertainties in the enhanced time-distance plot

The time-distance plot was taken by averaging over three pixels across the slit, therefore the data noise as in Eq. (3) should be scaled by a factor of $1/\sqrt{3} = 0.58$. The running difference was generated by $R(s_m, t_k) = C(s_m, t_k) - C(s_m, t_{k-9})$. We assumed the images were taken independently, there was no data noise correlation along the time sequence. For a value in the running difference plot, the uncertainty is estimated as $\sigma(R(s_m, t_k)) = \sqrt{\sigma^2(C(s_m, t_k)) + \sigma^2(C(s_m, t_{k-9}))}$. The noise amplitude in the running difference plot can be estimated with Eq. (1). On average, it is ~0.4% of the background intensity and ~30% of the amplitude of the propagating disturbances.

The background is constructed by averaging over $N = 50$ points. The uncertainty in $B(s_m, t_k)$ is $1/\sqrt{50 \times 3}$ of a normal flux value, and hence is neglected. Thus $\sigma(D(s_m, t_k)) = \sigma(C(s_m, t_k))/B(s_m, t_k)$. It is ~0.3% of the background intensity and ~20% of the disturbance amplitude.

4. The measurement of the apparent phase speed

In the analysed dataset, propagating disturbances are seen at distances of less than ~20 Mm. Also, the apparent propagation speed appears constant at these distances. It is consistent with previous observations of this phenomenon, which showed that any noticeable speed variation can appear at larger heights only (Robbrecht et al. 2001; Gupta et al. 2010). No other periodicities, except 3-min oscillations, are found in the power spectrum of the time signal. We designed three methods for measuring the apparent speed of propagating disturbances, taking the observed fact that the phase speed in the sample does not change either with time or spatial location along the cut. Accordingly, we approximated the propagating disturbances with a propagating harmonic wave function $A\cos(\omega t - kx + \phi)$, with constant parameters A, ω, k and ϕ, which is the key element in the three methods:

– cross-fitting technique (CFT, Sect. 4.1);
– 2D coupled fitting (DCF, Sect. 4.2);
– best similarity match (BSM, Sect. 4.3).

We describe the methods in detail in the following subsections and apply the methods to the samples R_1 (D_1) and R_2 (D_2).

4.1. Cross-fitting technique

We assumed that the enhanced time-distance plot $X(s_m, t_k)$ is well described by $A\cos(\omega t - kx + \phi)$. At each spatial location (pixel), the variation of the pixel flux $X(s_m, *)$[1] is taken as a time series. The errors $\sigma(X(s_m, *))$ are estimated as in Sect. 3.2. The time series is then fitted with $A_s\cos(\omega_s t + \phi_s) + \delta_s$[2]. Thus, the value of ω_s and its uncertainty[3] are obtained for each pixel. This is repeated for every pixel. The weighted mean and its uncertainty are calculated from abundant measurements (see top right panels of Figs. 3a,c,b and d). For each time sample, the spatial pixel flux variation $X(*, t_k)$ along the direction of propagating disturbances is fitted with $A_t\cos(k_t x + \phi_t) + \delta_t$ to obtain

the wave number. By repeating this operation for each pixel, we are able to get a weighted mean of k (see bottom left panels of Figs. 3a,c,b and d). Finally, the parameters ω and k, with their weighted means, are combined to calculate the phase speed (see bottom right panels of Figs. 3a,c,b and d).

We performed the Levenberg-Marquardt least-squares minimisation using the function *mpfitfun.pro* provided by Markwardt (2009). We applied constraints on the amplitude in the fitting, the $A_{t,s}$ are bounded between A_w and $\sqrt{2}A_w$, based on the fact that the root mean square of the wave $A\cos(\omega t - kx + \phi)$ is $A/\sqrt{2}$. The results are displayed in Fig. 3 and summarised in Sect. 5.

4.2. 2D coupled fitting

Similarly to CFT, we assumed that the signal is of a harmonic form. Instead of performing independent non-linear fitting in both axes, we performed global 2D fitting with the function $A\cos(\omega t - kx + \phi) + \delta$.

We applied the same non-linear fitting algorithm: the Levenberg-Marquardt least-squares minimisation, using the 2D fitting function *mpfit2dfun.pro* provided by Markwardt (2009). Similarly to CFT, we constrained the amplitude between A_w and $\sqrt{2}A_w$. The results are illustrated in Fig. 4 and described in Sect. 5.

4.3. Best similarity match

The enhanced time-distance plot can be regarded as an image with tilted ridges, which can be roughly described by the harmonic propagating function $A\cos(\omega t - kx + \phi)$. We are able to measure the propagating speed and period by shape matching between the enhanced time-distance plot and a model image $M(s_m, t_k) = A\cos(\omega t_k - ks_m + \phi)$. The shape matching is quantified by a similarity measure, which is mostly based on the Minkowski distance $L_p(M, R) = \left(\sum_{m=1}^{m=N_s} \sum_{k=1}^{k=N_t} |M(s_m, t_k) - X(s_m, t_k)|^p \right)^{1/p}$, where p is a positive number whose values ranges from 1 to ∞ depending on a specific definition. We calculated the Euclidean distance ($p = 2$) to find the similarity measure. If images M and R match exactly, $L_p = 0$, otherwise, the best similarity measure is found by minimising L_p.

In our case, let $X = X(s_m, t_k)$ be R_1 (D_1) or R_2 (D_2) (and is referred to as the reference image hereafter), and construct the model image M with the model function of the same size as X. The amplitude of M was scaled by a factor $\langle X \rangle / \langle M \rangle$, where $\langle \ldots \rangle$ means rms, so that M and X have approximately the same amplitude.

The model image $M = M_{P, V_p, \phi}(s_m, t_k)$ is parametrised by the period $P = 2\pi/\omega$, apparent phase speed $V_p = \omega/k$ and phase ϕ. We set $P \in [150, 200]$ s in 1 s step, $V_p \in [20, 120]$ km s^{-1} in 1 km s^{-1} step, and $\phi \in [0, 2\pi]$ in 5 degree step. For every combination of P, V_p and ϕ, a model image is constructed and the associated Minkowski distance $L_p(R, M_{P, V_p, \phi})$ is calculated. By locating $L_p^{\min}$ in the parametric space, we are able to find the best combination of P, V_p and ϕ, these are the parameters that we need to measure R. We accepted 1% above the $L_p^{\min}$, and took a set of P, V_p and ϕ, with the means and standard deviations as the observed value and their uncertainties. The application of BSM to R_1 (D_1) and R_2 (D_2) is shown in Fig. 5.
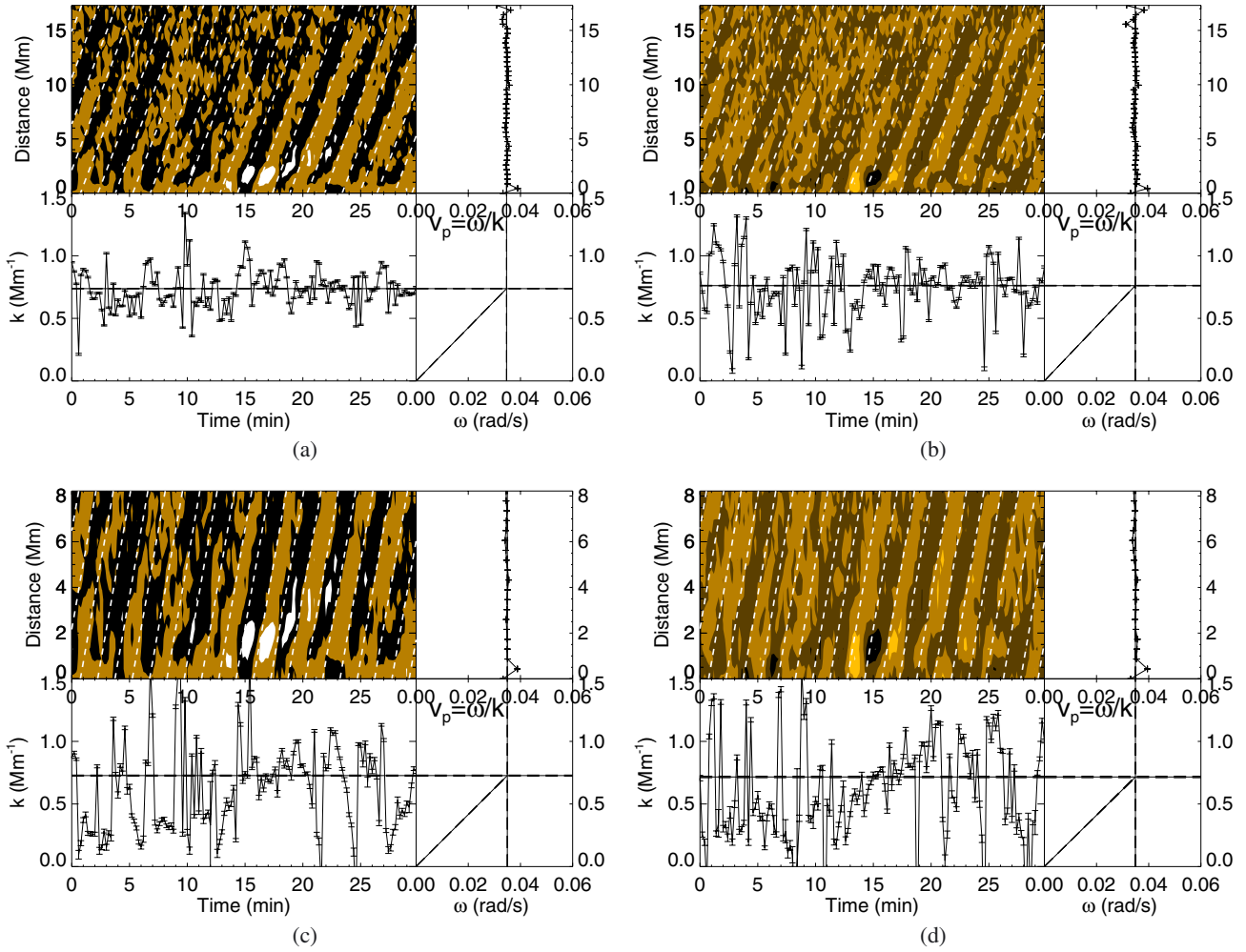
---

[1] $X(s_m, *)$ means that taking the samples in the array $X(s_m, t_k)$ at indices $(s_m, 1)$, $(s_m, 2)$, $\cdots$, (s_m, N_t), while $X(*, t_k)$ means sampling at $(t_k, 1)$, $(t_k, 2)$, $\cdots$, (t_k, N_s) as in the following text.
[2] The subscript s denotes that this parameter varies with the spatial location s, an extra term δ_s allows for weak fluctuations between the pixels.
[3] We take 4σ as the uncertainty at 99.99% confidence level throughout the paper, unless otherwise specified.

Fig. 3. Application of CFT to R_1 **a)**, R_2 **c)**, D_1 **b)**, and D_2 **d)**. In each panel, *top left*: the running difference of the time-distance plot, overlaid with the contour (white dashed line) of the model function $A\cos(\omega t - kx + \phi)$ with the best-fitted parameters. *Top right*: the fitting result of ω as a function of the spatial location. The thick solid line is the weighted mean, the dashed lines indicate its uncertainties. *Bottom left*: the fitting result of k as a function of time. The thick solid line is the weighted mean, and the dashed lines indicate its uncertainties. *Bottom right*: the ω-k dispersion diagram and the calculation of phase speed V_p and its uncertainties. The fitted parameters are as follows: **a)** for R_1, $\omega = 0.0347 \pm 0.00002$ rad/s, $k = 0.738 \pm 0.002$ Mm^{-1}, $P = 181.2 \pm 0.1$ s, $V_p = 47.0 \pm 0.1$ km s^{-1}; **c)** for R_2 $\omega = 0.0350 \pm 0.00003$ rad/s, $k = 0.727 \pm 0.005$ Mm^{-1}, $P = 179.7 \pm 0.2$ s, $V_p = 48.1 \pm 0.3$ km s^{-1}; **b)** for D_1 $\omega = 0.0349 \pm 0.00003$ rad/s, $k = 0.762 \pm 0.00$ Mm^{-1}, $P = 180.0 \pm 0.1$ s, $V_p = 45.8 \pm 0.2$ km s^{-1}; **d)** for D_2 $\omega = 0.0349 \pm 0.00003$ rad/s, $k = 0.716 \pm 0.006$ Mm^{-1}, $P = 180.0 \pm 0.2$ s, $V_p = 48.6 \pm 0.4$ km s^{-1}.

The shape matching can generally be improved by the image regularisation (smoothing). For an image $I(x, y)$, the regularised image can be obtained by its convolution with a normalised Gaussian kernel, $I_{\sigma_x, \sigma_y} = I(x, y) * G(\sigma_x, \sigma_y)$. In our case, neither R_1 (D_1) nor R_2 (D_2) have enough pixels to perform smoothing without severely subjecting to the edge effect, therefore we only regularised the image with a three-point discrete Gaussian kernel along the time axis. The resulting images R_1^σ (D_1^σ) and R_2^σ (D_2^σ) are displayed in Fig. 6. The ridge pattern looks clearer than in Fig. 5. The effect of regularisation on the measurement of BSM will be discussed in Sect. 5.

5. Results

We applied CFT to the sample R_1 (Fig. 3a). The fits of ω have a relative error lower than 1% and are distributed in a very narrow band. The weighted mean gives $\omega = 0.0347 \pm 0.00002$ rad/s, which corresponds to a period of $P = 181.2 \pm 0.1$ s. Fits to k has a relative error of $\lesssim 10\%$. The weighted mean $k = 0.738 \pm 0.002$ Mm^{-1} has a relative error of less than 1%, and

the values scatter about $\pm 50\%$ of the mean. Thus the apparent phase speed is calculated as $V_p = 47.0 \pm 0.1$ km s^{-1}. The resulting propagating features are overlaid with R_1 as the white dashed line in the top left panel of Fig. 3a. The spacing (P) matches very well, implying good fits to ω, the slope V_p of the dashed lines deviates slightly from the well recognised ridges, while remaining in the acceptable range.

We shortened the spatial length of the sample and applied CFT to R_2. The spatial length of R_2 is a half of R_1, but it includes the most prominent part of the ridges that represents the propagating disturbances. The results are shown in Fig. 3c. The rise of the relative error in k to above 10% is due to the decrease in the number of data points in the spatial direction, therefore the constraint on k is loosed. As seen in Fig. 3c, the best-fitting values of k are distributed in a broader range than those obtained for R_1. The weighted mean of k is about $k = 0.727 \pm 0.005$ Mm^{-1}. The measure of ω retains a good accuracy ($\omega = 0.0350 \pm 0.00003$ rad/s, $P = 179.7 \pm 0.2$ s), which is slightly worsened because of the decrease in the number of samples. The phase speed is calculated as $V_p = 48.1 \pm 0.3$ km s^{-1}.
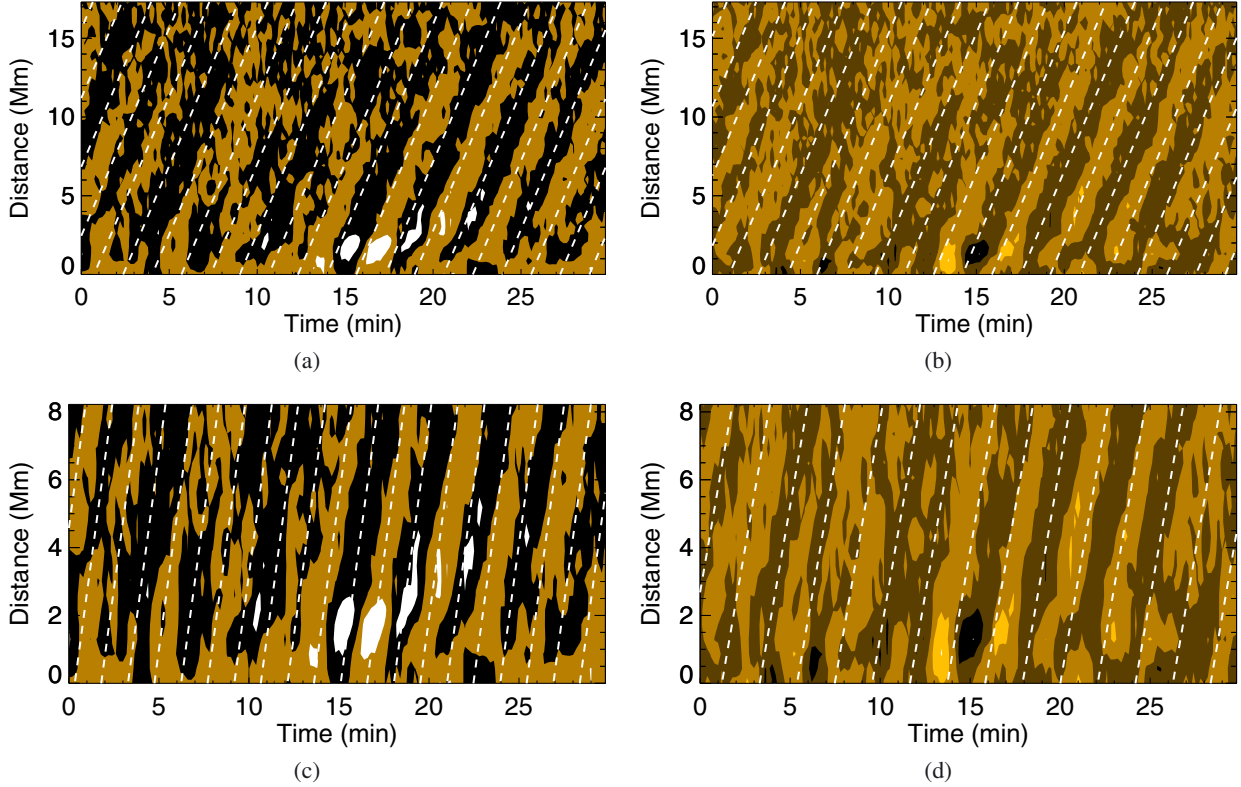
Fig. 4. Application of DCF to R_1 **a)**, R_2 **c)**, D_1 **b)**, and D_2 **d)**. In each panel, the running difference of the time-distance plot is overlaid with the contour (white dashed line) of the model function $A\cos(\omega t - kx + \phi)$ with the best-fitted parameters. The best-fitted parameters are: **a)** for R_1, $P = 240.7 \pm 0.7$ s, $V_p = 48.8 \pm 0.2$ km s^{-1}; **c)** for R_2, $P = 177.2 \pm 0.9$ s, $V_p = 65.8 \pm 0.3$ km s^{-1}; **b)** for D_1, $P = 198.9 \pm 0.7$ s, $V_p = 44.5 \pm 0.2$ km s^{-1}; **d)** for D_2, $P = 250.5 \pm 2.2$ s, $V_p = 51.4 \pm 0.5$ km s^{-1}.

The spacing remains consistent with the running difference as illustrated in the top left panel of Fig. 3c, the alignment is also very good.

Applying CFT to D_1 and D_2 with a higher signal-to-noise ratio (S/N) gives $V_p = 45.8 \pm 0.2$ km s^{-1} and $P = 180.0 \pm 0.1$ s and $V_p = 48.6 \pm 0.4$ km s^{-1} and $P = 180.0 \pm 0.2$ s, respectively. Both fits are acceptable, and consistent with those obtained for R_1 and R_2.

The application of DCF to R_1 (D_1) and R_2 (D_2) is displayed in Figs. 4a,b and Figs. 4c,d. The fit values are listed in Table 2. The DCF is very sensitive to the initial guess for the fit parameters. Since 2D fitting is coupled in both axes, the optimised fit can be reached only for one of the parameters. In our case, we optimised the fit of V_p, by changing the initial guess. It can be optimised for P as well. A fully automatic fit is not feasible because of the dependence on the initial guess.

The BSM works well for all variants of the sample: R_1 (D_1), R_2 (D_2), and the regularised samples R_1^σ (D_1^σ), R_2^σ (D_2^σ), as illustrated in Figs. 5 and 6. The measurements are summarised in Table 2. The measurement of P and V_p are persistently good in all samples. It appears that BSM is very robust and not sensitive to any pre-processing of the sample.

5.1. The effect of lag time

The choice of the lag time ($T_\text{lag} = l \times$ cadence) determines the quality of the running difference plot. Our choice of $l = 9$ applied above is just a specific case that appears to be in a good range of selection. To illustrate the effect of the lag time constructing the running-difference data set on the method performance, we

Table 2. Comparison of the measured results of the CFT, DCF and BSM methods.

		CFT	DCF	BSM
R_1	P (s)	181.2 ± 0.1	240.7 ± 0.7	180.0 ± 1.8
	V_p (km s^{-1})	47.0 ± 0.1	48.8 ± 0.2	47.0 ± 2.6
R_2	P (s)	179.7 ± 0.2	177.2 ± 0.9	178.0 ± 2.0
	V_p km s^{-1}	48.1 ± 0.3	65.8 ± 0.3	49.0 ± 4.5
R_1^σ	P (s)	...	...	180.0 ± 1.0
	V_p km s^{-1}	...	...	48.0 ± 1.3
R_2^σ	P (s)	...	...	180.0 ± 1.0
	V_p (km s^{-1})	...	...	50.0 ± 2.6
D_1	P (s)	180.0 ± 0.1	198.9 ± 0.7	180.0 ± 1.0
	V_p (km s^{-1})	45.8 ± 0.2	44.5 ± 0.2	47.0 ± 1.4
D_2	P (s)	180.0 ± 0.2	250.5 ± 2.2	178.0 ± 1.0
	V_p km s^{-1}	48.6 ± 0.4	51.4 ± 0.5	49.0 ± 2.8
D_1^σ	P (s)	...	...	180.0 ± 1.0
	V_p km s^{-1}	...	...	48.0 ± 1.3
D_2^σ	P (s)	...	...	180.0 ± 0.9
	V_p (km s^{-1})	...	...	50.0 ± 2.3

plot the measurements of CFT, BSM and BSM(σ) as a function of the lag time in the left columns of Fig. 8a[4] (R_1) and Fig. 8b[4] (R_2). The results of DCF are omitted due to its sensitivity to the initial guess. Clearly, for R_1, the measurements of V_p and P are consistently good with the lag time ranging from 12 s to 156 s.

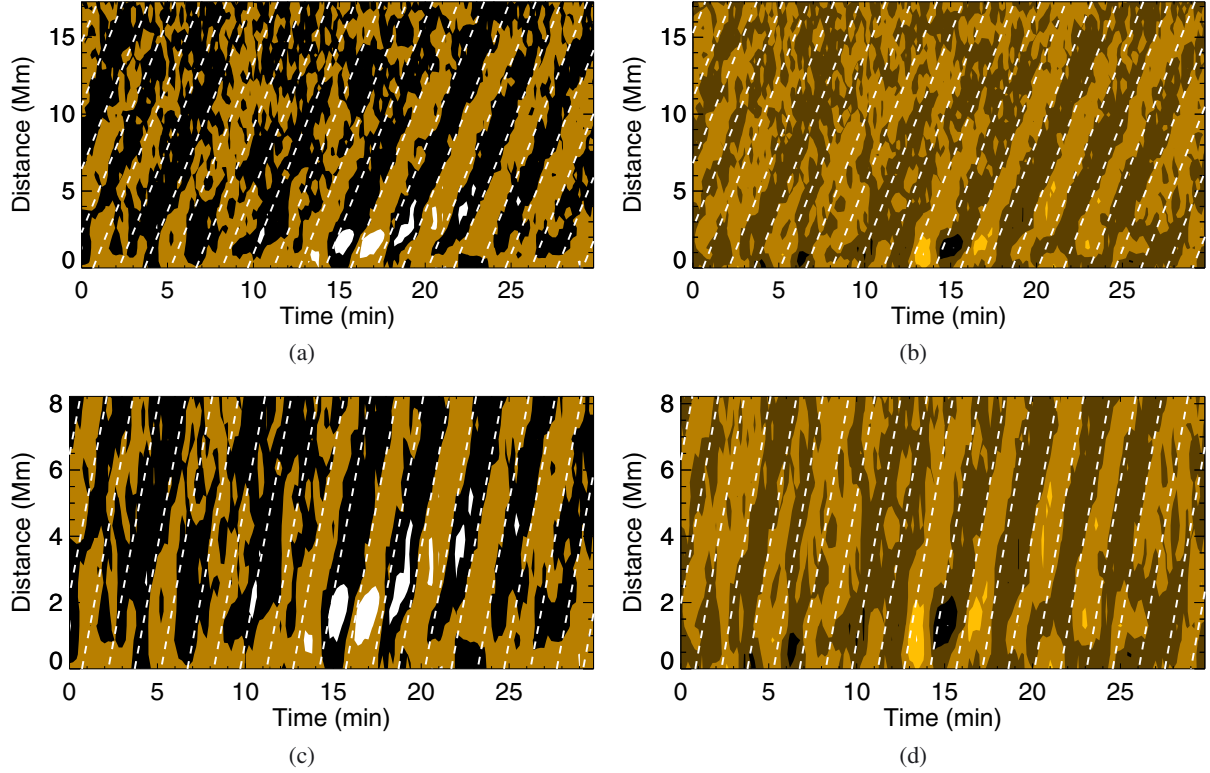[4] A complete set of figures displaying the quality of the measurements is available at

http://www2.warwick.ac.uk/fac/sci/physics/research/cfsa/people/yuan

Fig. 5. Application of BSM to R_1 **a)**, R_2 **c)**, D_1 **b)**, and D_2 **d)**. In each panel, the running difference of the time-distance plot is overlaid with the contour (white dashed line) of the model function $A\cos(\omega t - kx + \phi)$ with the fitted parameters. The fitted parameters are as follows: **a)** for R_1, $P = 180.0 \pm 1.8$ s, $V_p = 47.0 \pm 2.6$ km s^{-1}; **c)** for R_2, $P = 178.0 \pm 2.0$ s, $V_p = 49.0 \pm 4.5$ km s^{-1}; **b)** for D_1, $P = 180.0 \pm 1.0$ s, $V_p = 47.0 \pm 1.4$ km s^{-1}; **d)** for D_2, $P = 178.0 \pm 1.0$ s, $V_p = 49.0 \pm 2.8$ km s^{-1}.
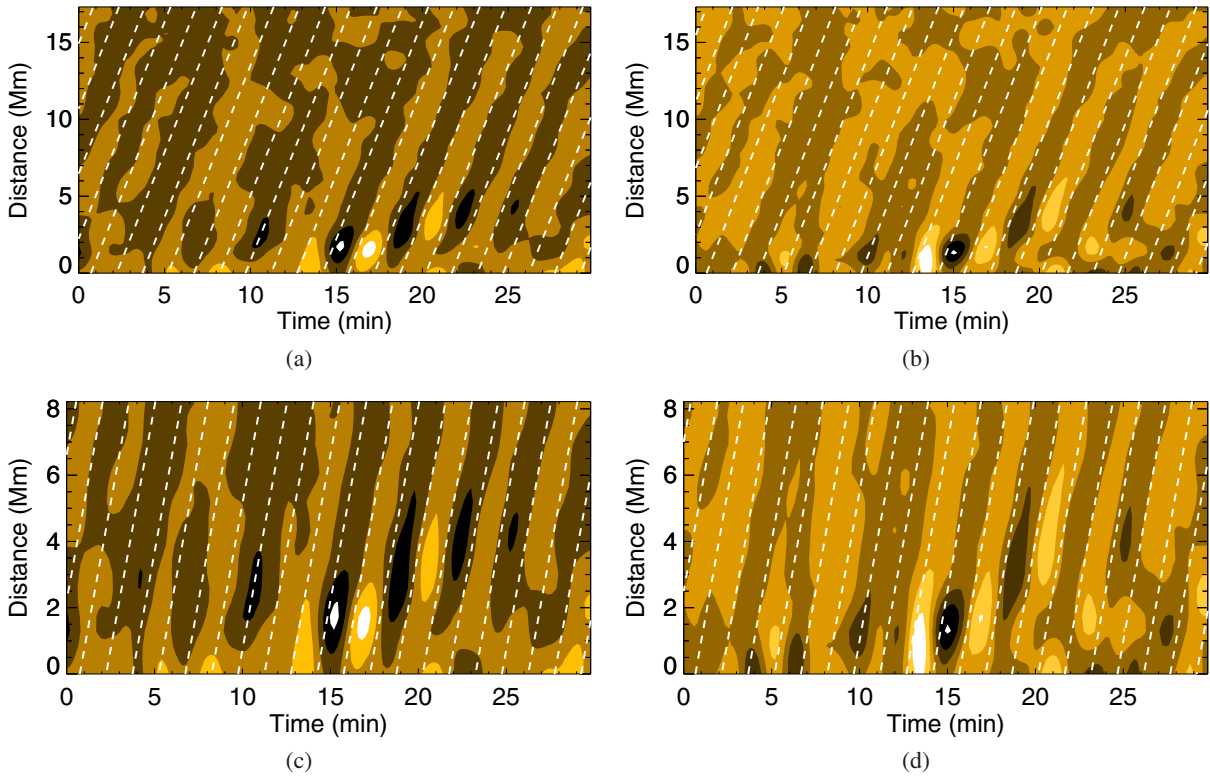

Fig. 6. Application of BSM to R_1^σ **a)**, R_2^σ **c)**, D_1^σ **b)**, and D_2^σ **d)**. In each panel, the running difference of the time-distance plot is overlaid with the contour (white dashed line) of the model function $A\cos(\omega t - kx + \phi)$ with the best-fitted parameters. The best-fitted parameters are follows: **a)** for R_1^σ, $P = 180.0 \pm 1.0$ s, $V_p = 48.0 \pm 1.3$ km s^{-1}; **c)** for R_2^σ, $P = 180.0 \pm 1.0$ s, $V_p = 50.0 \pm 2.6$ km s^{-1}; **b)** for D_1^σ, $P = 180.0 \pm 1.0$ s, $V_p = 48.0 \pm 1.3$ km s^{-1}; **d)** for D_2^σ, $P = 180.0 \pm 0.9$ s, $V_p = 50.0 \pm 2.3$ km s^{-1}.
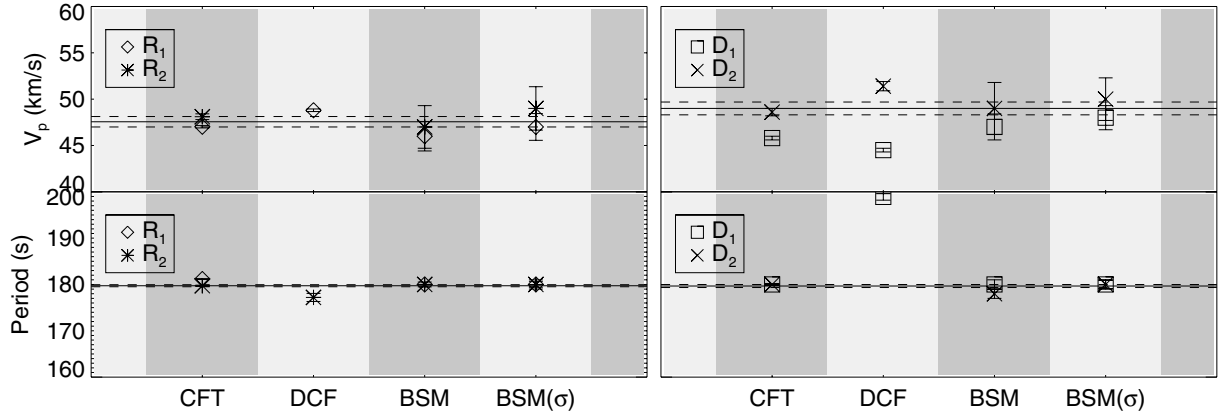
Fig. 7. Comparison of the measurements obtained with CFT, DCF, BSM and BSM(σ). V_p and P are plotted in the upper and lower panels, respectively. The solid line is the corresponding average value and the dashed lines enclose the uncertainty of 1σ range in each panel. For R_1 ($\diamond$) and R_2 ($\ast$), $\bar{V}_p = 47.6 \pm 0.6$ km s^{-1} and $\bar{P} = 179.7 \pm 0.2$ s. For D_1 ($\square$) and D_2 ($\times$), $\bar{V}_p = 49.0 \pm 0.7$ km s^{-1} and $\bar{P} = 179.7 \pm 0.3$ s.
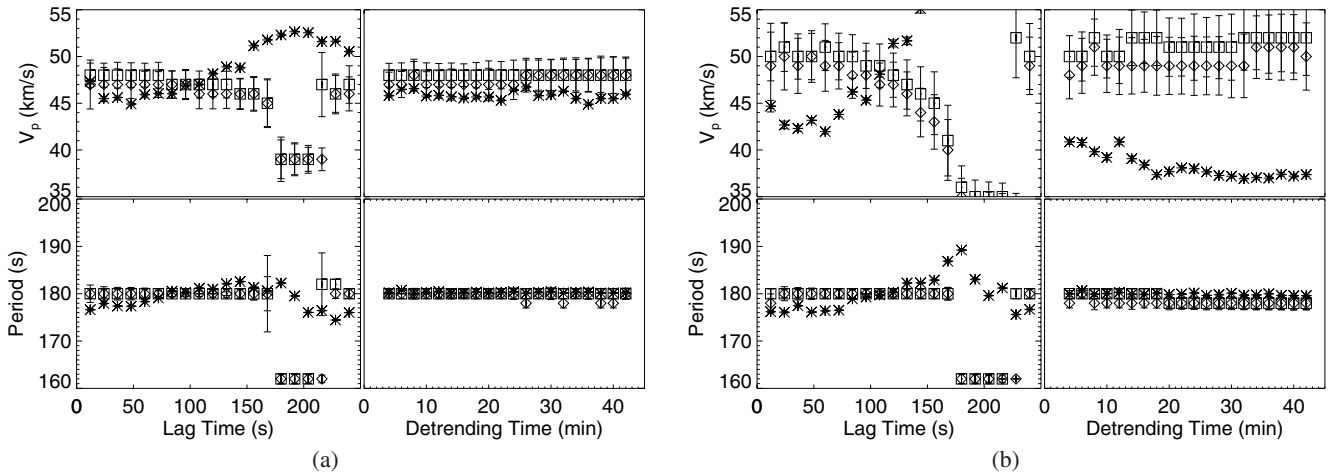

Fig. 8. a) Measurement of the phase speed and period in R_1 as a function of the lag time, and those in D_1 as a function of the smoothing time. **b)** The corresponding measurement in R_2 and D_2. In **a)** and **b)**, the *upper panel* is the measurement of V_p and the *bottom* one is of P. The measurements obtained with CFT, BSM and BSM (σ) are shown in $\ast$, $\diamond$ and $\square$ respectively.

However, for the shorter sample R_2, the selection of the lag time is more constrained within 84 s and 132 s, within which the quality of ridges is optimised. This means that for samples with a larger spatial length the choice of the lag time is less limited than for shorter ones.

5.2. The effect of detrending time

For the time-distance plot with the background removal and normalisation, the detrending time ($T_{\text{detr}} = N \times$ cadence) affects the results as well. We plot the measurements of CFT, BSM and BSM(σ) as a function of the detrending time in the right columns of Fig. 8a[4] (D_1) and Fig. 8b[4] (D_2). For D_1, the measurements are consistently good for all choices of the detrending time. It appears that the detrending time affects the results very little, while for those of D_2, the period P is measured very well with CFT, BSM and BSM (σ) in the whole range. For V_p, the measurements obtained with CFT are systematically lower than those of BSM and BSM(σ). The error bars of the BSM and BSM(σ) measurements are larger than those in D_1.

6. Conclusion

We designed three methods, CFT, DFC and BSM, to measure the average apparent phase speed of propagating EUV disturbances.

The applications to R_1 (D_1), R_2 (D_2), R_1^{σ} (D_1^{σ}), R_2^{σ} (D_2^{σ}) are summarised in Table 2 and illustrated in Fig. 7. Figure 8 shows the effect of the lag time and detrending time on the measurements.

From the computational aspect, the CPU time consumption descends as BSM, CFT, DCF. Applying these methods to $R_1(R_2)$ in a GNU/linux x86_64 computer, it takes 321(158) s, 4.9(2.5) s and 2.5(0.7) s for BSM, CFT and DCF, respectively. The CPU time consumption for D_1 and D_2 are very similar. In addition, CFT and DCF require estimating the data noise, but provide better accuracy. Also, the DCF is very sensitive to the initial guess for the parameters in the fitting function, therefore it is not suitable for automatic measurements (see, e.g. Sych et al. 2010; Martens et al. 2012). The BSM is more tolerant to the data noise and pre-operations that do not affect the image morphology.

The valid measurements of the apparent phase speed V_p in the analysed event range from 48 to 52 km s^{-1}, with an average value of 47.6 ± 0.6 km s^{-1} and 49.0 ± 0.7 km s^{-1} for $R_1(R_2)$ and D_1 (D_2), respectively (see Table 2 and Fig. 7, top panel).

For all three methods, it appears that the measurements made for R_1 and D_1 are on average better than those for R_2 and D_2. Accordingly, spatially-longer cuts, even if the amplitude of the disturbance is continuously declining, are preferable for the analysis. Longer samples are more tolerant to the

choice of the lag time and detrending time, while shorter ones restrict the choice. We also showed that the measurements in D_1 (D_2) generally outperform those made in R_1 (R_2), therefore the background-removal method seems to be superior than running difference, at least in our applications.

The measurements of the oscillating period are consistent in all methods and agree well with the measurements based upon spectral methods (e.g. Fourier transform or periodogram). Therefore, the methods described in the paper provide also an alternative tool for the estimation of the period.

The systematic error in the apparent phase speed estimation mainly originates from the traits of the propagating disturbance. In particular, the apparent phase speed may change along the propagating direction because of the geometry, projection or (and) physics, so that the diagonal ridges may be bent. But in the analysed case, the spatial scale of the detection of the propagating disturbances does not reach ~20 Mm, above which a noticeable change of propagating speed was reported (e.g. Robbrecht et al. 2001; Gupta et al. 2010). It may also be a variant of time, so different ridges do not have the same slope. In the analysed data we did not find this effect. Another deviation may originate from the inconsistency with the harmonic wave feature in our assumption. The good agreement in the measurement with the propagating harmonic wave form also implies that the propagating disturbances are slow magnetoacoustic waves rather than recurring upflows. The designed methods are not likely to work on samples taken during transient, e.g. flaring activity.

The amplitude A of the disturbance decreases during its travelling. The methods can be improved by accounting for the spatial variation of the amplitude $A = A(s_x)$. However, this will add an extra dimension to these methods, which means higher complexity. Another way of coping with this feature is to normalise the amplitude in each pixel along the cut to the highest amplitude of the narrowband signal measured at this pixel, before applying the methods.

Moreover, it is known that the amplitude of 3-min oscillations in sunspots is modulated by long-period oscillations (e.g. Sych et al. 2012). Therefore, it is natural to expect the same effect in their coronal counterpart observed in EUV. This effect can be studied with the methods designed in this paper, by applying them to a sliding window in time, imposed on a longer dataset. Likewise, the window can be applied in the spatial domain. This will reveal any possible speed variations in time and at different locations.

The three methods were shown to work well on the AIA data in EUV bandpasses. These methods can also be applied to other imaging data-cubes, obtained with other instruments and in other bands, e.g. UV, visible light and microwave.

References

Aschwanden, M. J., Nightingale, R. W., Tarbell, T. D., & Wolfson, C. J. 2000, ApJ, 535, 1027
Banerjee, D., Gupta, G. R., & Teriaca, L. 2011, Space Sci. Rev., 158, 267
Bel, N., & Leroy, B. 1977, A&A, 55, 239
Berghmans, D., & Clette, F. 1999, Sol. Phys., 186, 207
Boerner, P., Edwards, C., Lemen, J., et al. 2012, Sol. Phys., 275, 41
Botha, G. J. J., Arber, T. D., Nakariakov, V. M., & Zhugzhda, Y. D. 2011, ApJ, 728, 84
De Moortel, I. 2006, Roy. Soc. London Philos. Trans. Ser. A, 364, 461
De Moortel, I. 2009, Space Sci. Rev., 149, 65
De Moortel, I., & Hood, A. W. 2003, A&A, 408, 755
De Moortel, I., Ireland, J., & Walsh, R. W. 2000, A&A, 355, L23
De Moortel, I., Hood, A. W., Ireland, J., & Walsh, R. W. 2002a, Sol. Phys., 209, 89
De Moortel, I., Ireland, J., Walsh, R. W., & Hood, A. W. 2002b, Sol. Phys., 209, 61
De Pontieu, B., & McIntosh, S. W. 2010, ApJ, 722, 1013
De Pontieu, B., Erdélyi, R., & De Moortel, I. 2005, ApJ, 624, L61
Deforest, C. E., & Gurman, J. B. 1998, ApJ, 501, L217
Del Zanna, G. 2008, A&A, 481, L49
Doschek, G. A., Mariska, J. T., Warren, H. P., et al. 2007, ApJ, 667, L109
Doschek, G. A., Warren, H. P., Mariska, J. T., et al. 2008, ApJ, 686, 1362
Gupta, G. R., Banerjee, D., Teriaca, L., Imada, S., & Solanki, S. 2010, ApJ, 718, 11
Handy, B. N., Acton, L. W., Kankelborg, C. C., et al. 1999, Sol. Phys., 187, 229
Hara, H., Watanabe, T., Harra, L. K., et al. 2008, ApJ, 678, L67
Harra, L. K., Sakao, T., Mandrini, C. H., et al. 2008, ApJ, 676, L147
King, D. B., Nakariakov, V. M., Deluca, E. E., Golub, L., & McClements, K. G. 2003, A&A, 404, L1
Klimchuk, J. A., Tanner, S. E. M., & De Moortel, I. 2004, ApJ, 616, 1232
Krishna Prasad, S., Banerjee, D., & Gupta, G. R. 2011, A&A, 528, L4
Lemen, J. R., Title, A. M., Akin, D. J., et al. 2011, Sol. Phys., 172
Mariska, J. T., & Muglach, K. 2010, ApJ, 713, 573
Markwardt, C. B. 2009, in ASP Conf. Ser. 411, ed. D. A. Bohlender, D. Durand, & P. Dowler, 251
Marsh, M. S., Walsh, R. W., De Moortel, I., & Ireland, J. 2003, A&A, 404, L37
Marsh, M. S., Walsh, R. W., & Plunkett, S. 2009, ApJ, 697, 1674
Martens, P. C. H., Attrill, G. D. R., Davey, A. R., et al. 2012, Sol. Phys., 275, 79
Martínez-Sykora, J., De Pontieu, B., Hansteen, V., & McIntosh, S. W. 2011, ApJ, 732, 84
McIntosh, S. W., de Pontieu, B., & Tomczyk, S. 2008, Sol. Phys., 252, 321
Nakariakov, V. M., Verwichte, E., Berghmans, D., & Robbrecht, E. 2000, A&A, 362, 1151
Ofman, L., & Wang, T. 2002, ApJ, 580, L85
Ofman, L., Nakariakov, V. M., & Deforest, C. E. 1999, ApJ, 514, 441
Ofman, L., Nakariakov, V. M., & Sehgal, N. 2000, ApJ, 533, 1071
Robbrecht, E., Verwichte, E., Berghmans, D., et al. 2001, A&A, 370, 591
Sakao, T., Kano, R., Narukage, N., et al. 2007, Science, 318, 1585
Shibasaki, K. 2001, ApJ, 550, 1113
Sych, R., Nakariakov, V. M., Karlicky, M., & Anfinogentov, S. 2009, A&A, 505, 791
Sych, R. A., Nakariakov, V. M., Anfinogentov, S. A., & Ofman, L. 2010, Sol. Phys., 266, 349
Sych, R., Zaqarashvili, T. V., Nakariakov, V. M., et al. 2012, A&A, 539, A23
Tian, H., McIntosh, S. W., & De Pontieu, B. 2011a, ApJ, 727, L37
Tian, H., McIntosh, S. W., De Pontieu, B., et al. 2011b, ApJ, 738, 18
Tsiklauri, D., & Nakariakov, V. M. 2001, A&A, 379, 1106
Verwichte, E., Marsh, M., Foullon, C., et al. 2010, ApJ, 724, L194
Wang, T. J., Ofman, L., & Davila, J. M. 2009a, ApJ, 696, 1448
Wang, T. J., Ofman, L., Davila, J. M., & Mariska, J. T. 2009b, A&A, 503, L25
Yuan, D., Nakariakov, V. M., Chorley, N., & Foullon, C. 2011, A&A, 533, A116